Endogenous optical biomarkers of normal and human papillomavirus immortalized epithelial cells

Claudia Mujat[1], Cherry Greiner[1], Amy Baldwin[2], Jonathan M. Levitt[1], Fenghua Tian[1], Lee A. Stucenski[1], Martin Hunter[1,3], Young L. Kim[4], Vadim Backman[4], Michael Feld[3], Karl Münger[2] and Irene Georgakoudi[1,5*]

[1]*Department of Biomedical Engineering, Tufts University, Medford, MA*
[2]*The Channing Laboratory, Brigham and Women's Hospital, Department of Medicine, Harvard Medical School, Boston, MA*
[3]*George R. Harrison Spectroscopy Laboratory, Massachusetts Institute of Technology, Cambridge, MA*
[4]*Department of Biomedical Engineering, Northwestern University, Evanston, IL*
[5]*Wellman Center for Photomedicine, Massachusetts General Hospital, Boston, MA*

Cellular transformation is associated with a number of phenotypic, cell biological, biochemical and metabolic alterations. The detection and classification of morphological cellular abnormalities represents the foundation of classical histopathology and remains an important mainstay in the clinic. More recently, significant effort is being expended towards the development of noninvasive modalities for the detection of cancer at an early stage, when therapeutic interventions are highly successful. Methods that rely on the detection of optical signatures represent one class of such approaches that have yielded promising results. In our study, we have applied two spectroscopic imaging approaches to systematically identify in a quantitative manner the fluorescence and light scattering signatures of subcellular abnormalities that are associated with cellular transformation. Notably, we find that tryptophan images reveal not only intensity but also localization differences between normal and human papillomavirus immortalized cells, possibly originating from changes in the expression, 3D packing and organization of proteins and protein-rich subcellular organelles. Additionally, we detect alterations in cellular metabolism through quantitative evaluation of the NADH, FAD fluorescence and the corresponding redox ratio. Finally, we use light scattering spectroscopy to identify differences in nuclear morphology and subcellular organization that occur from the nanometer to the micrometer scale. Thus, these optical approaches provide complementary biomarkers based on endogenous fluorescence and scattering cellular changes that occur at the molecular, biochemical and morphological level. Since they obviate the need for staining and tissue removal and can be easily combined, they provide desirable options for further clinical development and assessment.
© *2007 Wiley-Liss, Inc.*

Key words: cancer biomarkers; noninvasive imaging; cancer diagnosis; spectroscopy; fluorescence; light scattering; HPV; cervical cancer

Clinical cancer detection has relied heavily on the use of simple stains to visualize and classify morphological cellular abnormalities. The development of more sophisticated probes to evaluate specific oncogenic events continues to revolutionize early detection of various cancers. Nevertheless, a simple morphological evaluation of exfoliated cervical epithelial cells, the Papanicolaou ("Pap") smear has been exceedingly useful for detection of precancerous cervical lesions and may have saved more lives than any other commonly used cancer screening procedure. Many of the more sophisticated diagnostic tests involve physical removal of suspect tissue or other invasive or physically unpleasant procedures. Hence, the development of rapid, noninvasive methods is of paramount importance for successful early detection. Relatively simple spectroscopic procedures are available to measure alterations in a number of cellular parameters and may be well suited for this purpose.

Indeed, optical spectroscopy and imaging techniques exhibited promising sensitivity and specificity profiles for the detection of a number of epithelial neoplasias, including early or precancerous lesions in the cervix,[1–5] breast,[6–9] colon[10] and the esophagus.[11,12] Especially in the context of tissue fluorescence measurements, the origins or the onset of the optical changes that are correlated with cancer development are not fully understood and remain poorly characterized. Nevertheless, some key chromophores and their relative value for reporting relevant biochemical and molecular cell features are known. For example, NADH and FAD are two naturally fluorescing coenzymes that are involved in oxidative phosphorylation and can serve as reporters of metabolic activity.[13] Tryptophan, along with tyrosine and phenylalanine, are amino acids whose fluorescence can be used to quantify changes in protein expression, structure or microenvironment.[14,15]

More recently, light scattering has also been exploited as a source of contrast for spectroscopic imaging of cells and tissues. This approach relies on the fact that when light impinges upon matter whose refractive index is different from the surrounding medium, it will get scattered at different angles and wavelengths in a manner that is characteristic of the size (or size distribution), shape and refractive index of the sample. For example, lipid membranes and proteins have a higher refractive index than water and are expected to scatter light. Because protein complexes and numerous subcellular organelles are packed tightly within a cell, the wavelength and angle dependence of the scattered light can reveal information about the distribution of characteristic lengths over which different cellular components organize, when these dimensions are smaller or on the order of the wavelength of light that interacts with the cell (*i.e.,* at scales spanning tens of nanometers to approximately a micron). In fact, it has been found that refractive index fluctuations within cells and tissues have a fractal behavior, *i.e.,* they appear to have very similar patterns of organization when examined over a wide range of length scales, similar to the organization of snowflakes or coastlines.[16] For instance, a recent study has demonstrated that light scattering spectroscopy (LSS) can be used to acquire information about differences both in the overall level of organization and the length scales over which subcellular components organize in normal and dysplastic esophageal epithelial tissues.[17] In other cases, light scattering based approaches have been shown to detect similar types of changes in colonic epithelia even before molecular stains are able to reliably identify preneoplastic change.[10,18] For organelles such as nuclei, that are significantly larger than the wavelength of visible light, LSS can be used to extract specific information regarding their size, shape and refractive index. For example, LSS has been performed *in vivo* to detect noninvasively changes in nuclear morphology in dysplastic lesions in the esophagus, colon, oral cavity, bladder and the cervix.[3,11,19-21]

The goal of our study was to determine in a quantitative way the autofluorescence and light scattering signatures of normal and human papillomavirus (HPV)-immortalized human epithelial

keratinocytes, as a first step in understanding and modeling some of the complementary optical signatures of early neoplastic development that these two techniques offer on molecular, biochemical and morphological changes that occur at the cellular level. HPVs are associated with a large spectrum of epithelial lesions and malignancies. Infections with high risk HPVs contribute to more than 95% of cervical cancer cases,[22] and are a significant factor in other anogenital tract carcinomas as well as in head and neck cancers.[23] Because the molecular pathways involved in cervical cancer progression following HPV infection are also rendered dysfunctional in numerous other human solid tumors, our studies may ultimately contribute to the development of sensitive, noninvasive diagnostic tools not only for detection of HPV-associated lesions, but for epithelial cancers more generally.

Material and methods

Cell culture

Primary human foreskin keratinocytes (HFKs) were isolated from a pool of neonatal foreskins and cultured as described by Jones *et al.*[24] HFKs immortalized by transfection with a plasmid containing a head to tail dimer DNA (HKc/HPV16) were kindly provided by Drs. Kim E. Creek and Lucia Pirisi (University of South Carolina School of Medicine, Columbia, SC). The establishment and characteristics of this cell line (TGF-beta resistant, differentiation resistant HKc/HPV16 [HKc/DR]) have been described in detail previously.[25–27] Both cell lines were maintained in 100 mm × 20 mm tissue culture dishes (Falcon), using keratinocyte serum free media (KSFM, Invitrogen), supplemented with epidermal growth factor, bovine pituitary extract and 1% penicillin/streptomycin, 0.1% gentamicin, 0.2% fungizone. HFKs were passaged 1:5 once a week, for up to 4 weeks (Passage 5). HKc/DRs were passaged 1:5 once a week. All cells were maintained in a 37°C, 5% CO_2 incubator.

Autofluorescence imaging

For fluorescence measurements, cells were plated on a 25-mm glass or quartz (SPI Supplies) coverslip at a concentration of ~80,000 cells per coverslip, and imaged 24 hr later. To eliminate the effect of cell density on fluorescence and for comparison purposes, each coverslip was seeded with the same number of cells, determined to yield 70–80% confluency based on visual assessment of DIC images at 24 hr after seeding.

Tryptophan fluorescence images were acquired from cells plated on quartz coverslips using a modified upright Leitz Orthoplan UV microscope with a 100×, 1.2 numerical aperture (NA) UV objective, index matched with glycerol. Light from a 100 W Xenon lamp (Oriel) was filtered by a 285/25 nm bandpass exciter (Omega) and reflected on to the sample by a 315 nm longpass dichroic beamsplitter (Omega). Emission through a 365/50 nm bandpass filter (attributed to tryptophan fluorescence)[13] was imaged using a 1,024 × 255 pixel, 16 bit UV-enhanced CCD camera (Andor) with an acquisition time of 10 sec. While cell viability was not tested rigorously, the fact that the cell morphology did not change as a result of image exposure strongly suggests that cell viability was not greatly affected during our measurements. These long exposure times likely introduced minimal photobleaching (on the 10% level of the overall signal). However, since both HFK and HPV cells were exposed for the same duration, we do not expect that photobleaching affects the comparison of the 2 populations. Corrected tryptophan images were obtained by subtracting the background image of a clean quartz coverslip.

NADH and FAD fluorescence images were acquired using an Olympus IX71 inverted microscope with a 60×, 1.4 NA objective, index matched with oil. Throughout the manuscript, we use the notation NADH to denote fluorescence from both NADH and NADPH molecules, which have very similar fluorescence signatures. However, since the cellular content and fluorescence quantum efficiency of NADH are higher than that of NADPH, we

expect that our results indicate mostly changes in the concentration of NADH.[28] In addition, because the fluorescence quantum efficiency of bound NADH is significantly higher than that of unbound NADH and since the detected NADH is consistent with mitochondrial localization, we anticipate that the dominant detected signal arises from bound NADH. For NADH fluorescence imaging, we used a 365/20 nm bandpass exciter (Omega), a 380 nm longpass dichroic beamsplitter (Chroma) and 450/65 nm bandpass emission filter (Omega). A filter set consisting of a 455/50 nm bandpass exciter (Omega), a 460 nm longpass dichroic beamsplitter (Chroma) and a 520/40 nm bandpass emission filter (Omega) was used for FAD imaging. These cultured cells do not contain significant levels of highly cross-linked keratins since they are cultured under conditions that inhibit their differentiation. Thus, fluorescence emanating from cross-linked keratin is not expected to interfere with our NADH and FAD measurements. Fluorescence intensity was captured using a 12 bit 1,200 × 1,600 pixel RT SPOT Slider camera (Diagnostic Instruments). Image acquisition time was 2 sec for NADH and FAD with 2 × 2 binning. We do not expect any effects on the viability of the cells for such short exposure times, since we have exposed cells for significantly longer times (4–6 sec) without any visible effects on morphology.

Angular LSS

For light scattering measurements, cells were suspended in 1 ml of KSFM ($\approx 1.8 \times 10^6$ cells/ml) and transferred to an attofluor cell chamber (Molecular Probes) equipped with a 25-mm (#1.5) glass coverslip. The cells were allowed to settle for ~5 min forming 3–4 layers on the coverslip and were analyzed using an angular light scattering spectroscopy (ALSS) system described in detail previously.[18] All measurements were performed with cells that had reached ~80% confluency as assessed by DIC inspection of the culture dish.

ALSS uses a backscattering geometry to acquire the angularly resolved, singly scattered intensity of the cells under investigation. Polarization gating is used to reject light that has been multiply scattered inside the sample; light incident on the sample is linearly polarized and the backscattered light is detected through an analyzer that can be placed either parallel (I_{par}) or perpendicular (I_{perp}) to the polarizer. Light that is scattered once maintains the original polarization, while light that has been multiply scattered is depolarized and consists of equal intensities along the parallel and perpendicular polarization orientations. Thus, the differential signal $\Delta I = I_{par} - I_{perp}$ can be used to select only singly scattered light.

Backscattered intensity maps were acquired from cells and background, for scattering angles between $-3.2°$ and $3.6°$, at wavelengths ranging from 450 to 700 nm, for both positions of the analyzer. The size of the illumination beam was ~5 mm in diameter, shedding light on ~200,000 cells stacked in 3–4 layers. To account for the angular and spectral effects induced by the lamp properties, the transmission of the optical components, the spectrograph grating characteristics and the camera quantum efficiency, scattered intensity maps were also obtained from a 99% reflection standard (LabSphere). Finally, the scattered intensity map of each cell sample was calculated as $\Delta I = \frac{I_{par\,cells} - I_{par\,bkg}}{I_{par\,standard}} - \frac{I_{perp\,cells} - I_{perp\,bkg}}{I_{perp\,standard}}$. The presence of multiple cell layers as opposed to a monolayer for these measurements yielded an enhancement in the level of detected backscattering signal. Nevertheless, single scattering remained the dominant contributor based on the fact that the intensity along the perpendicular polarization was significantly lower than that along the parallel polarization.

Data analysis

Matlab-based algorithms were developed to quantify the mean intensity of autofluorescence images. In the case of tryptophan, thresholding was performed to isolate the cellular regions, and it was followed by background subtraction to compare mean pixel intensities for frames from multiple experiments. Analysis was

performed from experiments performed in at least 2 different days and from multiple cell fields from at least 2 different coverslips per group per experiment. A total of approximately 160 HFK and 190 HPV cells included in the mean tryptophan fluorescence intensity calculations. For the NADH and FAD fluorescence images, the cytoplasmic regions of all cells in the field of view were manually outlined to exclude the nuclear region from intensity calculations, since these two chromophores are predicted to be primarily localized in the cytoplasm. The mean NADH or FAD intensity per pixel per cell was subsequently calculated. We analyzed images from experiments performed in two distinct days, with each experiment including cells from at least 3 coverslips and 10 fields per coverslip. There were ∼300 cells from each group included in the mean NADH, FAD and redox fluorescence intensity calculations.

A Mie scattering-based algorithm, necessary for fitting the light scattering results, was also developed on the Matlab platform based on the code initially described by Bohren and Hoffman.[29] Look-up tables that included the wavelength and scattering angle dependence of the backscattered light intensity for ranges that matched our experimental set-up (λ = 450–700 nm; θ = −3.2° to 3.6°) were generated for particle distributions with an inverse power-law ($N(d) = N_0 d^{-\beta}$) and a normal ($N(d) = \frac{1}{\sigma\sqrt{2\pi}}\exp\left[-\left((d - d_0)^2/2\sigma^2\right)\right]$) dependence on particle size, with $N(d)$ being the concentration of scattering particles with diameter d and σ the standard deviation of the distribution. For the inverse power-law distributions, light scattering patterns were simulated for populations with minimum scattering sizes between 0.01 and 0.05 μm (d_{min}) in 0.01 μm steps and maximum scattering sizes between 0.5 and 2 μm (d_{max}) in 0.1 μm steps. For each d_{min} and d_{max} combination, the refractive index contrast was changed from 1.01 to 1.09, with a step size of 0.01. For the normal distribution simulations, we considered populations with mean scattering center sizes between 3 and 25 μm (0.5 μm step) diameters, standard deviations of 0.0–25% of the diameter value (0.05% steps), and refractive index contrast varying between 1.04 and 1.09 (0.01 step size). The experimental light scattering spectra were compared to each one of these simulations through a χ^2 calculation. The best fit was chosen to correspond to the simulation yielding the minimum χ^2 value. This analysis approach of ALSS data acquired from a mixture of 50 nm and 5 μm beads yielding similar levels of signal as the small scatterers and nuclei of the cells, respectively, resulted in good agreement with theoretical results.

Cell staining

To asses the localization of tryptophan in the endoplasmic reticulum (ER), live HFK and HKc/DR cells were stained using 1 mM stock solution of the ER-Tracker[TM] Blue-White DPX dye (Molecular Probes) for 20 minutes. Images of stained cells were acquired with the same UV microscope and objective used in tryptophan fluorescence imaging, and a filter set including a 365/50 nm bandpass exciter (Omega), a 400 nm longpass dichroic beamsplitter (Omega) and a 545/90 nm bandpass emission filter (Omega). The upright microscope configuration prohibited ER-tracker imaging from coverslips that were also used for tryptophan imaging.

For studying the colocalization of NADH and FAD with metabolizing mitochondria in live cells, HFK and HKc/DR cells were stained with 1 mM MitoTracker[®] Orange (Molecular Probes) for 20 min. MitoTracker images were acquired for 15 msec, using the inverted Olympus IX71 microscope and a filter set including a 540/25 nm bandpass (Chroma) exciter, a 565 nm longpass dichroic beamsplitter (Chroma) and a 580 nm longpass emission filter (Chroma). Following acquisition of NADH and FAD images, the coverslip was removed from the stage, stained with Mito-Tracker and placed back in its original location. A custom made steel plate secured on the microscope stage allowed for precise repositioning of the attofluor chamber.

For nuclear morphological studies, 3.5×10^5 cells were plated on 25 mm (#1.5) glass coverslips and stained 24 hr later with

3 μg/ml acridine orange (Invitrogen) in KSFM for 5 min. The coverslip was then imaged with a Leica TCS SP2 confocal microscope. Confocal fluorescence imaging (488 nm excitation; 510–570 nm emission) with a 63×, 1.2 NA water-immersion objective was used to determine both the cross-sectional and the longitudinal diameter of HFK and HKc/DR cells. The cross sectional diameter (d_{cs}) was defined as the average between the largest and the smallest diameter of the nuclear cross-section, while the longitudinal diameter (d_l) was obtained by measuring a series of fluorescent images at different depths. Both diameters are defined at 20% of the peak fluorescence intensity, and averaged over at least 50 cells per group.

Redox ratio calculation

To accurately determine the redox ratios, the detected NADH and FAD autofluorescence intensity was converted to molar concentration by using a previously described procedure.[30] Specifically, fluorescence intensity calibration curves for NADH and FAD were obtained by imaging for 1 sec standard solutions of each fluorophore at different concentrations. The linear range used for fitting the fluorescence intensity calibration curve was 4–90 μM for FAD in Hank's balanced salt solution buffer and 10–215 μM for NADH bound to alcohol dehydrogenase, which closely resembles NADH in its cellular environment.[30] From the generated fluorescence intensity calibration curves, the mean fluorophore concentration in the cells was determined based on the mean intensity of the background corrected cell images. The corresponding redox ratio was calculated from the NADH and FAD concentrations as $\frac{[FAD]}{[NADH]+[FAD]}$. A standard 2-tailed Student's t-test was subsequently used to assess differences in the redox ratios at a significance level of $p < 0.05$. Even though the concentration calibrations were not performed at each experiment day, we do not expect day to day throughput variations to affect the resulting redox ratios, since NADH and FAD should be affected equally and such variations would cancel out during the redox ratio estimations. In addition, we have only observed background level intensity variations only on the order of 2–3% throughout the course of this experiment, indicating consistent levels of performance.

Results

Tryptophan fluorescence intensity and localization in normal and HPV-immortalized cells

Tryptophan autofluorescence can be used as a sensitive, general indicator of protein expression in cells. To determine whether this parameter is altered in HPV-immortalized epithelial cells, we acquired and analyzed tryptophan images of normal and HPV-immortalized keratinocytes using a UV microscope (Figs. 1a and 1b). As expected, the protein rich nucleolus exhibits strong tryptophan fluorescence for all cells. Interestingly however, the cytoplasmic localization pattern of tryptophan fluorescence appears different in the two cell populations. Specifically, normal HFKs exhibit a bright mesh-like network of tryptophan fluorescence, whereas the immortalized HKc/DR cells display a more diffuse localization pattern. Tryptophan is expected to localize preferentially within protein rich organelles, such as the endoplasmic reticulum (ER). Indeed, we detected ER staining that was similar to the observed tryptophan autofluorescence, with a well-defined meshwork visible only in the HFK population (Figs. 1c and 1d). These differences may represent changes in the intracellular membrane organization or in the architecture of protein complexes induced by HPV oncogene expression.

Quantitative analysis of the mean cellular tryptophan autofluorescence intensity reveals the presence of additional differences between the normal and HPV-immortalized cells. Specifically, as indicated in Table I, we find that the mean tryptophan intensity increases significantly when the cells transform to their immortalized state ($p < 0.05$). These differences are likely the result of a combination of alterations that can potentially occur during neoplastic transformation, including changes in the pH of the in-
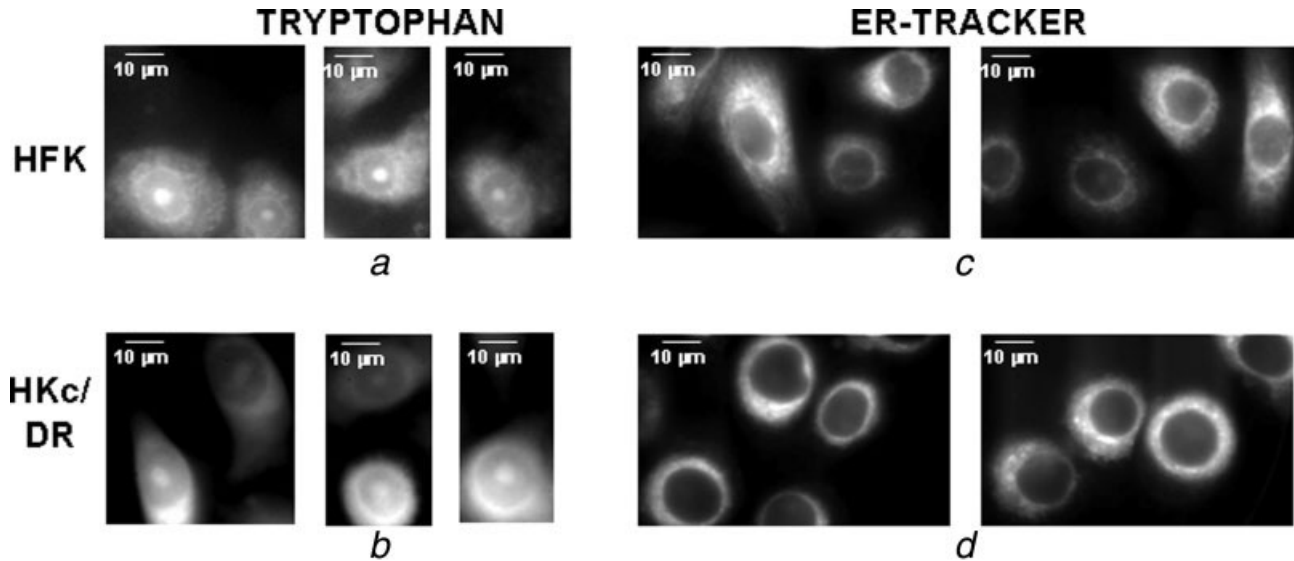
FIGURE 1 – Typical tryptophan (*a*, *b*) and ER tracker (*c*, *d*) fluorescence images for normal (*a*, *c*) and HPV-immortalized (*b*, *d*) human foreskin keratinocytes.

TABLE I – QUANTITATIVE ASSESSMENT OF THE FLUORESCENCE INTENSITY AND REDOX RATIO OF NORMAL AND HPV-IMMORTALIZED CELLS

Cell population	Tryptophan intensity per pixel (mean ± se)	NADH intensity per cell per pixel (mean ± se)	FAD intensity per cell per pixel (mean ± se)	Redox ratio per pixel per cell (mean ± se)
HFK	1450 ± 80	3553 ± 84	2021 ± 45	0.0290 ± 0.0006
HPV-immortalized	2065 ± 103	3725 ± 72	1870 ± 32	0.0250 ± 0.0004

tracellular environment, as well as in 3D protein conformation and overall protein expression levels.

NADH, FAD and redox images of normal and HPV-immortalized cells

NADH and FAD autofluorescence and the associated redox ratio, ([FAD]/([NADH]+[FAD]), have been exploited in a number of *in vitro* and *in vivo* studies for detecting changes in metabolic activity that are typically associated with neoplastic transformation.[31–34] Thus, we sought to examine the presence of differences in intensity or localization of these fluorophores between normal and HPV-immortalized cells. Representative examples of normal HFKs and HKc/DR cell images acquired at optimal excitation/emission wavelengths for detecting NADH (365/450 nm) and FAD (450/525 nm) fluorescence are shown in Figure 2. The fluorescence images of both cell populations show a dark nucleus with bright granular and/or tubular fluorescence throughout the cytoplasm. Since NADH and FAD are essential coenzymes involved in electron transfer for ATP production, these fluorophores are likely to be found in the mitochondria. Indeed, corresponding Mitotracker fluorescence images (Fig. 2) show excellent colocalization with autofluorescence excited at 365 and 455 nm, confirming that this endogenous fluorescence is primarily found in the active metabolizing mitochondria, and is, thus, consistent with fluorescence emanating from NADH and FAD.

Unlike tryptophan, we find that the patterns of NADH and FAD fluorescence localization are similar for the normal and HPV-immortalized cells. However, significant differences are present in the mean cellular intensity of these chromophores. Specifically, as indicated in Table I, we find that NADH fluorescence increases by ~5% ($p < 0.10$), while FAD fluorescence decreases by more than 7% ($p < 0.05$). These changes lead to an overall significant decrease ($p < 0.05$) of over 13% in the redox ratio of the HPV-immortalized cells, which in turn represents an increase in the overall metabolic activity of these cells compared to the normal keratinocytes.[35] In addition, a 2-tailed squared ranks test has indi-

cated that the level of variance observed in the NADH and FAD fluorescence intensities for the two populations of cells is statistically different ($p < 0.0001$).

Light scattering spectroscopic signatures of subcellular components

Although traditional histopathological evaluation of neoplastic changes has focused on morphological changes of the nuclear size, shape and chromatic density (*i.e.,* the amount of stain that is taken up by the nuclear material), more recent studies have indicated that the overall organization of material within cells and tissues changes with neoplastic transformation.[10,17,18] Such studies have been primarily based on detection and analysis of refractive index variations and the use of fractal-based models to describe the organization and packing of the material. For our study, we acquired angular and wavelength dependent maps of the singly backscattered intensity of light from the normal and HPV-transformed cells. Representative examples of such maps are included in Figures 3a and 3b. Although the general backscattering features of the two cell populations are similar, the spectral map in Figure 3c, which represents the ratio of intensities detected from the HFK and HKc/DR cells, shows that both the angular and the wavelength decay of the intensity is steeper for the HFK cells.

We illustrate quantitatively this wavelength dependence in Figures 3d and 3e for two different samples of each cell population at a backscattering angle of 0°. The intensity of light decreases monotonically with increasing wavelength, and the decay rate is slower for the HPV-immortalized than the normal cells. The wavelength dependence of the backscattered intensity from both cell types obeys a power law decay $\Delta I(\lambda) \propto \lambda^{-\gamma}$, with average γ values of 1.62 for HFKs and 1.28 for the HPV cells, as shown in Figure 3f. This difference suggests packing of cell membranes and protein complexes within larger overall units that are less organized in the HPV-immortalized cells than in the normal cells.

To describe these changes in a more quantitative manner, we modeled the cellular components that yield the detected scattered
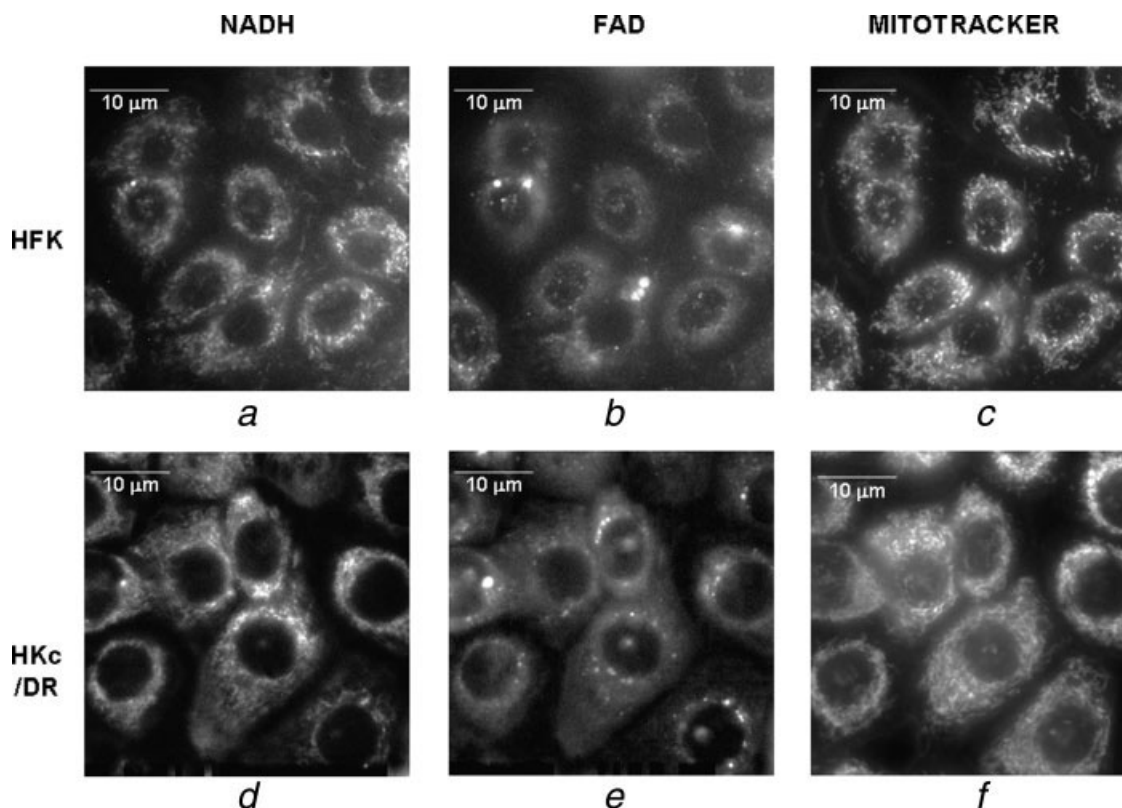
FIGURE 2 – Typical NADH (*a, d*), FAD (*b, e*) and MitoTracker (*c, f*) fluorescence images for normal (*a, b, c*) and HPV-immortalized (*d, e, f*) human foreskin keratinocytes.

light by a distribution of discrete spherical particles, whose radius could vary from 10 nm to 2 μm, relevant for the observed wavelength dependence of the scattered light. This distribution had an inverse power-law dependence on the particle size, such that $N(d) = N_0 d^{-\beta}$, where $N(d)$ is the number of particles with diameter d, N_0 is a constant and β is a size independent coefficient. The exponent β is related to the exponent of the intensity decay simply by the relationship $\beta = 3 + \gamma$ (based on Mie theory simulations), and thus, it is equal to 4.62 and 4.28 for HFKs and HKc/DRs, respectively. Consistent with these studies, we show in Figure 4*a* that scattering from such a distribution of sizes modeled by Mie theory can describe accurately the experimental intensity decays. On the basis of a χ^2 minimization fitting procedure, we determined that the distribution of scattering particles that best recovered the power law decay of the backscattered intensity was 0.03–1.2 μm for the normal keratinocytes and 0.04–2 μm for the HPV-immortalized cells, at an average refractive index contrast of 1.06 (Fig. 4*b*). The range of sizes that characterize both types of cells is indeed representative of protein complexes, membranes and subcellular organelles, with the transformed cells including scatterers that are organized in significantly larger units. These would imply a more "clumped" appearance for the subcellular organization of the HPV-cells, that is consistent with one of the histopathological hallmarks of precancers of hematoxylin and eosin stained sections.

We should note that Mie theory together with a power law distribution of scatterers predict a flat angular dependence of the backscattered intensity, while our experimental results show higher intensity in the exact backscattering direction for both cell populations. This discrepancy may be explained by the fact that the cell scattering structures are not perfect spheres, as assumed by the Mie model.

Light scattering spectroscopic signatures of cell nuclei

It has been previously shown that the wavelength dependence of the backscattered intensity is also related to the nuclear size of the cells.[3,11,19,36] For the cell populations that we examined, the dominant contribution to the detected backscattered light originates from subcellular organelles with characteristic sizes that are smaller than the size of the nucleus. For a more accurate characterization of the nuclear morphology, we performed 3D confocal imaging of the cells incubated with a nuclear stain (acridine orange). As summarized in Table II, these imaging studies indicate that the cross-sectional nuclear diameter (*i.e.,* the diameter parallel to the plane of the acquired images) for the cultured HKc/DR cells ($d_{cs} = 14.71 \pm 2.86$ μm) is larger than the corresponding dimension in the HFKs ($d_{cs} = 11.87 \pm 1.95$ μm). However, as indicated in the insets of Figures 4*c* and 4*d*, the longitudinal diameter (*i.e.,* the diameter perpendicular to the plane of the images) of the cultured HPV-immortalized cells ($d_l = 4.6 \pm 0.46$ μm) is almost half the longitudinal diameter of the HFKs ($d_l = 8.85 \pm 1.08$ μm). Thus, in both cases the nuclear shape deviates significantly from a sphere, with the HPV immortalized cells having a much flatter pancake-like morphology.

To determine whether any particles from these range of dimensions contributed to the observed light scattering spectra, we focused on the residual spectra acquired following subtraction of the modeled fits achieved by the power-law scatterer distribution model from the acquired light scattering spectra included in Figures 4*a* and 4*b*. Such residual spectra are shown in Figure 4*c* and 4*d* and exhibit significantly different features for the normal and HPV-immortalized cells. These light scattering spectra can be described using a Mie theory-based scattering model that includes a normal distribution of scatterers, with the corresponding best fits also plotted in Figure 4*c* and 4*d*. The mean diameters and standard deviations of the particle distributions that resulted in the best fit to these residual light scattering spectra are 7.25 ± 0.275 μm for the HFKs and 4.38 ± 0.437 μm for the HPV-immortalized cells (Table II), with average refractive index contrast of 1.05 and 1.055, respectively. Thus, the observed light scattering spectra
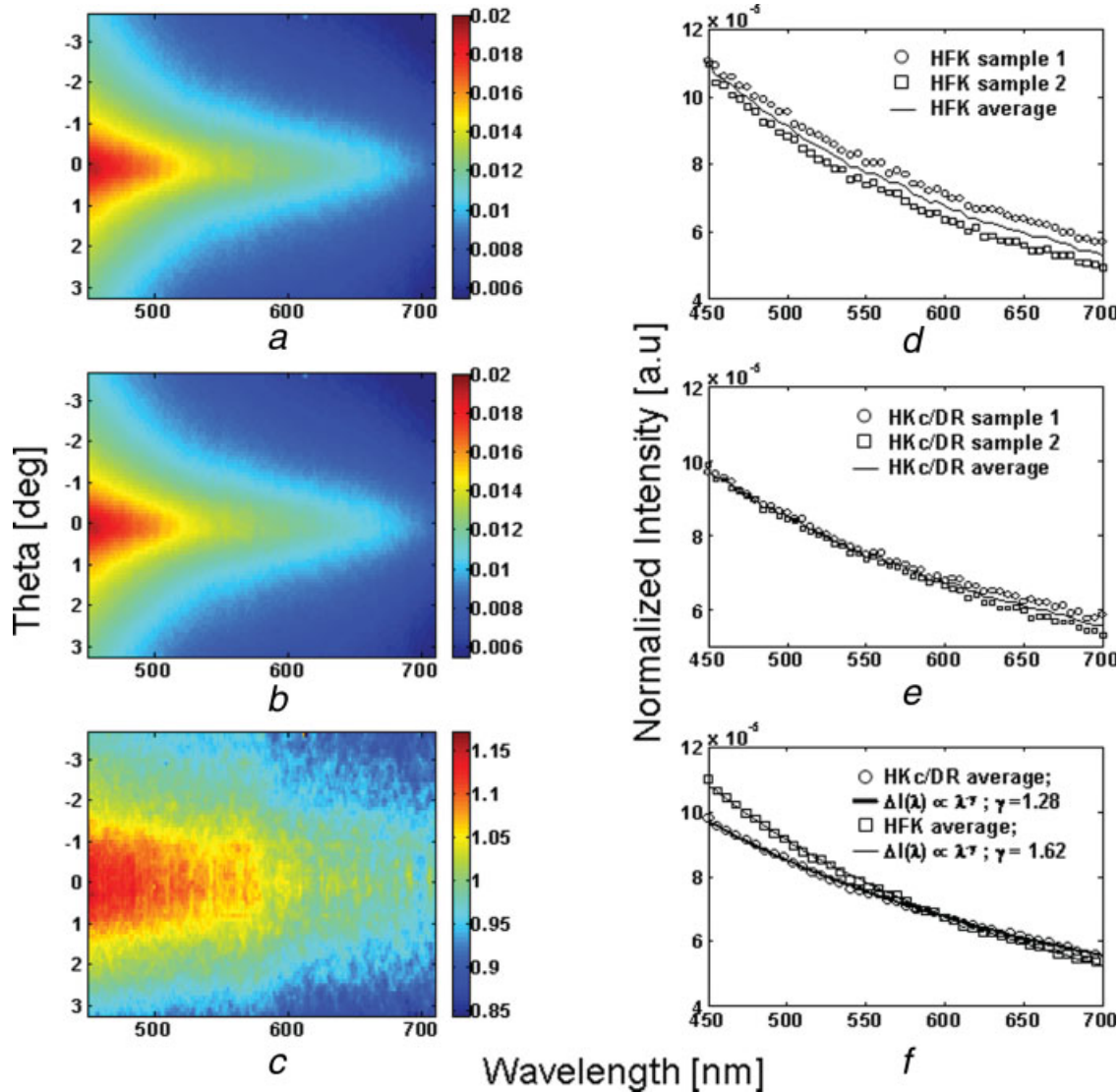
FIGURE 3 – Angular and wavelength dependent maps of the backscattered intensity (θ = −3.2°–3.6°; λ = 450–700 nm) for normal HFK (*a*) and immortalized HKc/DR cells (*b*). (*c*) The light scattering map representing the ratio of the backscattered light from the normal and immortalized cells demonstrates the presence of differences between the 2 cell populations. Examples of wavelength dependent backscattered intensity decays at θ = 0 from 2 distinct cell samples, as well as a mean spectrum are shown for the normal (*d*) and immortalized (*e*) cells. (*f*) Comparison of mean wavelength-dependent light scattering spectra at θ = 0 for normal (open circles) and HPV-immortalized (open squares) cells, along with the corresponding fits (solid lines) to $\Delta I(\lambda) \propto \lambda^{-\gamma}$. Average γ is 1.62 for HFKs and 1.28 for the HKc/DR cells.

also include information about significant changes in the longitudinal diameter of the nuclei of the cells under investigation. This is important, because changes in nuclear morphology represent some of the major histopathological hallmarks confirming the presence of precancerous and cancerous lesions.

Discussion

In our study, we present the first comprehensive, quantitative investigation of the endogenous fluorescence and light scattering properties of normal and HPV16-immortalized epithelial cells as a model of the cellular optical changes that occur during the development of precancerous epithelial lesions. We demonstrate that significant differences are present in the localization and intensity of fluorescent chromophores such as tryptophan (Fig. 1), NAD(P)H and FAD (Fig. 2). These differences represent alterations in the levels

of protein expression and metabolic activity that are induced by HPV-transfection and are consistent with the functions of the HPV E6 and E7 oncoproteins. In addition, our light scattering measurements report that not only the biochemistry but also the organization of the subcellular units (Figs. 3 and 4) and the nuclear morphology change (Fig. 4) appreciably in HPV-immortalized cells.

A number of interesting observations have arisen as a result of our study. For example, in one of very few studies presenting cellular tryptophan autofluorescence images, we show that changes not only in autofluorescence intensity but also in localization may accompany neoplastic transformation. The more diffuse tryptophan fluorescence detected in the HPV-immortalized cells could be the result of changes in the organization of subcellular membranes and organelles or of protein complex conformational changes. These types of changes are also reported and quantitatively assessed by the wavelength-dependent light scattering spectra.
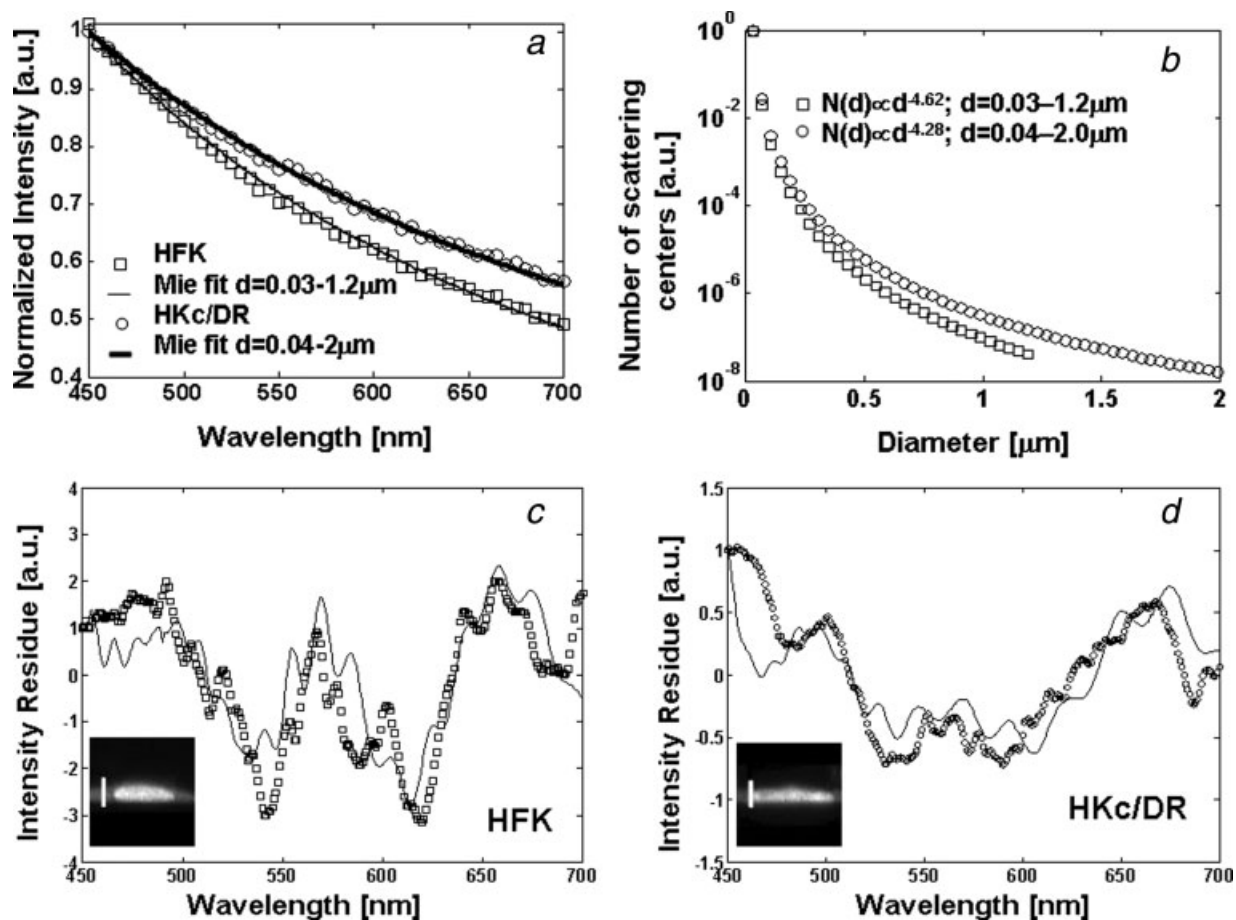
FIGURE 4 – (*a*) The wavelength-dependent light scattering spectra from normal (□, HFK) and HPV-immortalized (○, HKc/DR) cells are described well by a model that accounts for scattering from a distribution of spheres with an inverse power law dependence on the spheres' diameter ($N(d) \propto d^{-\beta}$) as indicated by the corresponding fits (thin solid line, HFK; thick solid line, HKc/DR). (*b*) The distributions of scattering sizes that correspond to the best fits for the spectra shown in panel (*a*) and correspond to β = 4.62; d = 0.03–1.2 μm for HFKs (□) and β = 4.28; d = 0.04–2 μm for HKc/DRs (○). (*c*, *d*) Residual spectra obtained after subtracting the power law fit from the experimental light scattering spectra for normal (*c*) and HPV-immortalized (*d*) cells along with the corresponding Mie fits (solid lines) acquired assuming a normal distribution of scatterer sizes.

TABLE II – NUCLEAR DIAMETERS OF THE HFK AND HPV CELLS OBTAINED BY MORPHOLOGICAL NUCLEAR STUDIES AND ALSS RESIDUE ANALYSIS

	Nuclear morphology			
	Cross-sectional nuclear diameter, d_{cs}[1] (μm)	Standard deviation of d_{cs} (μm)	Longitudinal nuclear diameter, d_{l}[2,3] (μm)	Standard deviation of d_{l} (μm)
HFK	11.87	1.95	8.85	1.08
HPV-immortalized	14.71	2.86	4.60	0.46

	ALSS residual analysis	
	Nuclear diameter, d_{ALSS} (μm)[4]	Standard deviation of d_{ALSS} (μm)
HFK	7.25	0.275
HPV-immortalized	4.38	0.437

[1]Defined as the average between the smallest and the largest diameter of the largest nuclear cross-section.–[2]Obtained by imaging the cultured cells at different depths.–[3]Defined at 20% of the peak fluorescence intensity.–[4]Obtained by fitting the backscattered intensity residuals with Mie scattering for normal distributions of sizes.

The intensity differences that we observe in tryptophan and NADH fluorescence are consistent with numerous studies comparing normal and (pre)cancerous cells or tissues in the cervix, lung, colon, bladder and metastatic melanoma.[2,3,14,31,37-39] We also cal-

culated the cellular redox ratio, *i.e.,* the ratio of FAD to the sum of NADH and FAD, as a more rigorous measure of aerobic glycolysis.[35] We found that the redox ratio of HPV-immortalized cells is significantly lower compared to that of normal epithelial cells

(Table I) and the level of this decrease was higher than the level of changes we detected in each of the fluorophores individually.

This decrease in the redox ratio corresponds to an increase in metabolic activity associated with HPV-induced transformation, which is consistent with loss of regulation of cell proliferation mediated by the action of the HPV16-E7 oncoprotein.[24] Metabolic alterations in HPV-immortalized cells may also be caused by association of pyruvate kinase with HPV16-E7, which has been shown to affect physiological regulation of pyruvate kinase[40] and/or activation of alpha-glucosidase,[41] which in turn results in depletion of glycogen stores. It is interesting to note that the level of difference that is detected for the two cell populations is enhanced when the information from both NADH and FAD is combined in the redox ratio calculation. Thus, our study indicates that this ratiometric approach may confer a higher level of sensitivity for detecting metabolic changes associated with neoplasia, in addition to offering a more rigorous method that accounts for potential day-to-day variations in instrument performance.

Changes in cellular pH may also affect directly or indirectly the detected levels of NADH and FAD autofluorescence. Transformed cells generally have a high intracellular pH and HPV E7 expressing NIH 3T3 cells exhibited increased activity of the Na^+/H^+ exchanger protein, resulting in cytoplasmic alkalinization. Inhibition of E7-induced alkalinization caused alterations in glycolytic metabolism and reduced several parameters of cellular transformation including proliferation, growth in low serum or anchorage independent growth.[42] These physiological abnormalities in E7-expressing cells may directly contribute to induction of cellular transformation, or they may reflect necessary metabolic adaptations to the altered energy requirements of rapidly proliferating transformed cells.

Complementary to the biochemical and metabolic changes reported by autofluorescence, light scattering spectroscopic studies reveal morphological and structural/organizational differences between normal and HPV-immortalized cells. The major contributor to the light scattered in the backward direction consists of protein complexes, subcellular membranes and organelles that are packed in larger, less organized units in the transformed cells. Cell nuclei also yield a small contribution to the detected scattering signals in a manner that is characteristic of the longitudinal but not the transverse diameter of the cells. There is good agreement between the light scattering- and confocal-based estimates of the mean value and standard deviation for the longitudinal diameter of the HPV cells, while both parameters are underestimated by the light scattering-based analysis for the norml HFKs. This may be due to differences in the actual morphology of the cells during the two types of measurements, since in the confocal case the cells were attached to the coverslip so that staining and washing could be performed, while in the light scattering case, cells were allowed to settle on the coverslip for a few minutes. This discrepancy may also arise from the use of a sphere-based model and our inability to extract the very weak nuclear light scattering signals accurately. An improved method for detecting the light scattered from the nucleus has been reported recently and will be further explored in the future.[43] Nevertheless, sensitivity of light scattering to the longitudinal and not to the cross-sectional nuclear diameter was also reported in another light scattering study that investigated nuclear morphology of T84 epithelial cells with Fourier domain low coherence interferometry.[44] Interestingly, we find through LSS and confocal microscopy that the longitudinal diameter of HPV-immortalized cells is significantly smaller than that of normal keratinocytes.

In summary, we demonstrate that the combination of multicolor fluorescence and light scattering imaging can be used to detect non-invasively a wide range of molecular, biochemical and morphological changes induced by HPV-transfection. While the optical changes we characterize in our study are likely representative of transformed cells in general, future studies will focus on the assessment of fluorescence and light scattering changes associated with the specific actions of the HPV E6 and E7 oncoproteins. Such studies will provide further insight into the cellular pathways that mediate these alterations. The complementary nature of the information provided by fluorescence and light-scattering-based methods in an entirely noninvasive manner presents an attractive and potentially very useful approach for studying the dynamic interdependence of cell biochemical and morphological features during the onset of neoplasia. Extending such imaging studies to depth-resolved modalities of 3D tissues will be important for improving our understanding of such processes in more sophisticated disease models. Ultimately, we expect that this knowledge will be transferred to the development and improvement of noninvasive tools for detecting pre-cancerous lesions in a highly sensitive and specific manner. It may also be possible to translate this type of measurements to examination of cell scrapings from Pap smears, especially in the context of the ALSS measurements; however, it is not clear yet how the differentiation and proliferation status as well as fixation of those cells would affect the corresponding fluorescence and light scattering signals.

References

1. Chang SK, Mirabal YN, Atkinson EN, Cox D, Malpica A, Follen M, Richards-Kortum R. Combined reflectance and fluorescence spectroscopy for in vivo detection of cervical pre-cancer. J Biomed Opt 2005;10:024031.
2. Drezek R, Brookner C, Pavlova I, Boiko I, Malpica A, Lotan R, Follen M, Richards-Kortum R. Autofluorescence microscopy of fresh cervical tissue sections reveals alterations in tissue biochemistry with dysplasia. Photochem Photobiol 2001;73:636–41.
3. Georgakoudi I, Sheets EE, Muller MG, Backman V, Crum CP, Badizadegan K, Dasari RR, Feld MS. Trimodal spectroscopy for the detection and characterization of cervical precancers in vivo. Am J Obstet Gynecol 2002;186:374–82.
4. Ramanujam N, Follen-Mitchell M, Mahadevan-Jansen A, Thomsen SL, Staerkel G, Malpica A, Wright T, Atkinson N, Richards-Kortum R. Cervical precancer detection using a multivariate statistical algorithm based on laser-induced fluorescence spectra at multiple excitation wavelengths. Photochem Photobiol 1996;64:720–35.
5. Milbourne A, Park SY, Benedet JL, Miller D, Ehlen T, Rhodes H, Malpica A, Matisic J, Van Niekirk D, Atkinson EN, Hadad N, Mackinnon N, et al. Results of a pilot study of multispectral digital colposcopy for the in vivo detection of cervical intraepithelial neoplasia. Gynecol Oncol 2005;99(3, Suppl 1):S67–S75.
6. Bigio I, Bown S, Briggs G, Kelley C, Lakhani S, Pickard D, Ripley P, Rose I, Saunders C. Diagnosis of breast cancer using elastic-scattering spectroscopy: preliminary clinical results. J Biomed Opt 2000;5:221–28.
7. Haka AS, Shafer-Peltier KE, Fitzmaurice M, Crowe J, Dasari RR, Feld MS. Diagnosing breast cancer by using Raman spectroscopy. Proc Natl Acad Sci USA 2005;102:12371–6.
8. Palmer GM, Zhu C, Breslin TM, Xu F, Gilchrist KW, Ramanujam N. Comparison of multiexcitation fluorescence and diffuse reflectance spectroscopy for the diagnosis of breast cancer (March 2003). IEEE Trans Biomed Eng 2003;50:1233–42.
9. Shah N, Cerussi AE, Jakubowski D, Hsiang D, Butler J, Tromberg BJ. The role of diffuse optical spectroscopy in the clinical management of breast cancer. Dis Markers 2003;19:95–105.
10. Roy HK, Liu Y, Wali RK, Kim YL, Kromine AK, Goldberg MJ, Backman V. Four-dimensional elastic light-scattering fingerprints as preneoplastic markers in the rat model of colon carcinogenesis. Gastroenterology 2004;126:1071–81; discussion 948.
11. Georgakoudi I, Jacobson B, Van Dam J, Backman V, Wallace MB, Müller MG, Zhang Q, Badizadegan K, Sun D, Thomas GA, Perelman LT, Feld MS. Fluorescence, reflectance and light scattering spectroscopy for evaluating dysplasia in patients with Barrett's esophagus. Gastroenterol 2001;120:1620–29.
12. Panjehpour M, Overholt B, Vo-Dinh T, Haggit R, Edwards D, Buckley F. Endoscopic fluorescence detection of high-grade dysplasia in Barrett's esophagus. Gastroenterol 1996;111:93–101.
13. Richards-Kortum R, Sevick-Muraca E. Quantitative optical spectroscopy for tissue diagnosis. Annu Rev Phys Chem 1996;47:555–606.

14. Anidjar M, Cussenot O, Avrillier S, Ettori D, Teillac P, Le Duc P. The role of laser-induced autofluorescence spectroscopy in bladder tumor detection. Ann NY Acad Sci 1998;838:130–42.

15. Yang Y, Celmer EJ, Zurawska-Szczepaniak M, Alfano RR. Excitation spectrum of malignant and benign breast tissues: a potential optical biopsy approach. Lasers Life Sci 1996;7:249–65.

16. Schmitt J, Kumar G. Turbulent nature of refractive-index variations in biological tissue. Opt Lett 1996;21:1210–312.

17. Hunter M, Backman V, Popescu G, Kalashnikov M, Boone CW, Wax A, Gopal V, Badizadegan K, Stoner GD, Feld MS. Tissue self-affinity and polarized light scattering in the born approximation: a new model for precancer detection. Phys Rev Lett 2006;97:138102.

18. Kim Y, Liu Y, Wali R, Roy H, Goldberg M, Kromin A, Chen K, Backman V. Simultaneous measurement of angular and spectral properties of light scattering for characterization of tissue microarchitecture and its alteration in early precancer. IEEE J Sel Top Quantum Electron 2003;9:243–56.

19. Backman V, Wallace MB, Perelman LT, Arendt JT, Gurjar R, Muller MG, Zhang Q, Zonios G, Kline E, McGilligan JA, Shapshay S, Valdez T, et al. Detection of preinvasive cancer cells. Nature 2000;406:35–6.

20. Müller MG, Valdez T, Georgakoudi I, Backman V, Fuentes C, Kabani S, Laver N, Wang Z, Boone C, Dasari R, Shapsay S, Feld MS. Spectroscopic detection and evaluation of morphologic and biochemical changes in early human oral carcinoma. Cancer 2003;97:1681–92.

21. Sokolov K, Drezek R, Gossage K, Richards-Kortum R. Reflectance spectroscopy with polarized light: is it sensitive to cellular and nuclear morphology? Opt Express 1999;5:302–17.

22. Bosch FX, Manos MM, Munoz N, Sherman M, Jansen AM, Peto J, Schiffman MH, Moreno V, Kurman R, Shah KV, Alihonou E, Bayo S, et al. Prevalence of human papillomavirus in cervical cancer: a world-wide perspective. J Nat Cancer Inst 1995;87:796–802.

23. Gillison ML, Koch WM, Capone RB, Spafford M, Westra WH, Wu L, Zahurak ML, Daniel RW, Viglione M, Symer DE, Shah KV, Sidransky D. Evidence for a causal association between human papillomavirus and a subset of head and neck cancers. J Natl Cancer Inst 2000;92:709–720.

24. Jones DL, Alani RM, Münger K. The human papillomavirus E7 oncoprotein can uncouple cellular differentiation and proliferation in human keratinocytes by abrogating p21^{Cip1}-mediated inhibition of cdk2. Genes Dev 1997;11:2101–11.

25. Khan MA, Jenkins GR, Tolleson WH, Creek KE, Pirisi L. Retinoic acid inhibition of human papillomavirus type 16-mediated transformation of human keratinocytes. Cancer Res 1993;53:905–9.

26. Khan MA, Tolleson WH, Gangemi JD, Pirisi L. Inhibition of growth, transformation, and expression of human papillomavirus type 16 E7 in human keratinocytes by α interferons. J Virol 1993;67:3396–403.

27. Pirisi L, Yasumoto S, Feller M, Doniger J, DiPaolo JA. Transformation of human fibroblasts and keratinocytes with human papillomavirus type 16 DNA. J Virol 1987;61:1061–6.

28. Vishwasrao HD, Heikal AA, Kasischke KA, Webb WW. Conformational dependence of intracellular NADH on metabolic state revealed by associated fluorescence anisotropy. J Biol Chem 2005;280:25119–26.

29. Bohren C, Hoffman D. Absorption and scattering of light by small particles. New York: Wiley, 1983.

30. Rocheleau JV, Head WS, Nicholson WE, Powers AC, Piston DW. Pancreatic islet β-cells transiently metabolize pyruvate. J Biol Chem 2002;277:30914–20.

31. Georgakoudi I, Jacobson BC, Müller MG, Badizadegan K, Carr-Locke DL, Sheets EE, Crum CP, Dasari RR, Van Dam J, Feld MS. NAD(P)H and collagen as in vivo quantitative biomarkers of epithelial pre-cancerous changes. Cancer Res 2002;62:682–7.

32. Levitt J, Baldwin A, Papadakis A, Puri S, Xylas J, Münger K, Georgakoudi I. Intrinsic fluorescence and redox changes associated with apoptosis of primary human epithelial cells. J Biomed Opt 2006;11:064012.

33. Pavlova I, Sokolov K, Drezek R, Malpica A, Follen M, Richards-Kortum R. Microanatomical and biochemical origins of normal and precancerous cervical autofluorescence using laser-scanning fluorescence confocal microscopy. Photochem Photobiol 2003;77:550–5.

34. Sud D, Zhong W, Beer DG, Mycek MA. Time-resolved optical imaging provides a molecular snapshot of altered metabolic function in living human cancer cell models. Opt Express 2006;14:4412–26.

35. Chance B, Cohen P, Jobsis F, Schoener B. Intracellular oxidation-reduction states in vivo. Science 1962;137:499–508.

36. Perelman L, Backman V, Wallace M, Zonios G, Manoharan R, Nusrat A, Shields S, Seiler M, Lima C, Hamano T, Itzkan I, Van Dam J, et al. Observation of periodic fine structure in reflectance from biological tissue: a new technique for measuring nuclear size distribution. Phys Rev Lett 1998;80:627–30.

37. Li BH, Xie SS. Autofluorescence excitation-emission matrices for diagnosis of colonic cancer. World J Gastroenterol 2005;11:3931–4.

38. Pradhan A, Pal P, Durocher G, Villeneuve L, Balassy A, Babai F, Gaboury L, Blanchard L. Steady state and time-resolved fluorescence properties of metastatic and non-metastatic malignant cells from different species. J Photochem Photobiol B 1995;31:101–12.

39. Ramanujam N, Mitchell M, Mahadevan A, Warren S, Thomsen S, Silva E, Richards-Kortum R. In vivo diagnosis of cervical intraepithelial neoplasia using 337-nm-excited laser-induced fluorescence. Proc Natl Acad Sci USA 1994;91:10193–97.

40. Mazurek S, Zwerschke W, Jansen-Durr P, Eigenbrodt E. Effects of the human papilloma virus HPV-16 E7 oncoprotein on glycolysis and glutaminolysis: role of pyruvate kinase type M2 and the glycolytic-enzyme complex. Biochem J 2001;356 (Part 1):247–56.

41. Zwerschke W, Mannhardt B, Massimi P, Nauenburg S, Pim D, Nickel W, Banks L, Reuser AJ, Jansen-Durr P. Allosteric activation of acid α-glucosidase by the human papillomavirus E7 protein. J Biol Chem 2000;275:9534–41.

42. Reshkin SJ, Bellizzi A, Caldeira S, Albarani V, Malanchi I, Poignee M, Alunni-Fabbroni M, Casavola V, Tommasino M. Na^{+}/H^{+} exchanger-dependent intracellular alkalinization is an early event in malignant transformation and plays an essential role in the development of subsequent transformation-associated phenotypes. FASEB J 2000;14:2185–97.

43. Yu CC, Lau C, Tunnell JW, Hunter M, Kalashnikov M, Fang-Yen C, Fulghum SF, Badizadegan K, Dasari RR, Feld MS. Assessing epithelial cell nuclear morphology by using azimuthal light scattering spectroscopy. Opt Lett 2006;31:3119–21.

44. Graf RN, Wax A. Nuclear morphology measurements using Fourier domain low coherence interferometry. Opt Express 2005;13:4693–98.